CrossMark

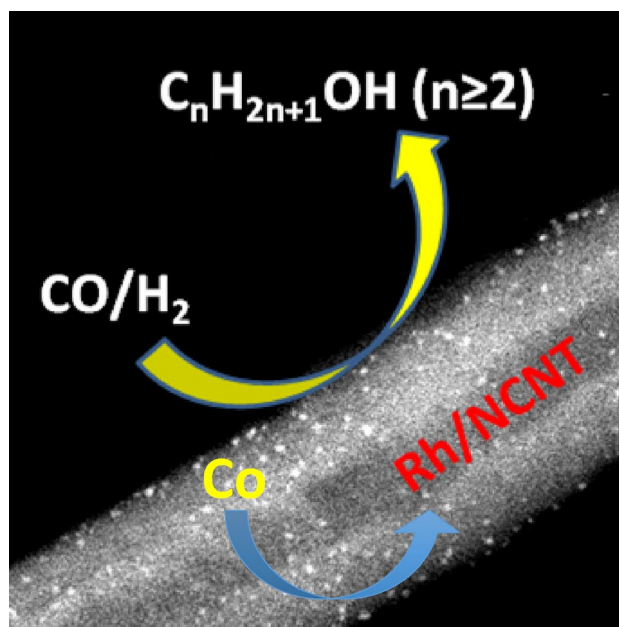# Higher Alcohol Synthesis Over Rh Catalysts: Conditioning of Rh/N-CNTs by Co and Mn Entrapped in the Support

Zailai Xie[1,2] · Benjamin Frank[1,3] · Xing Huang[1] · Robert Schlögl[1] ·
Annette Trunschke[1]

Abstract Rh nanoparticles supported on commercial non-purified N-doped CNTs (NCNTs) containing residual CNT growth catalyst have been studied in hydrogenation of CO to higher alcohols. It has been found that Co and Mn residues in NCNTs are not inert, but change the catalyst under reaction conditions and efficiently promote the catalyst resulting in both increasing activity and selectivity to C_{2+} alcohols with time on stream.

Graphical Abstract

Keywords Rhodium · Cobalt · Manganese · CNT growth catalyst · Higher alcohol synthesis · Carbon nanotubes · Nitrogen doping · Nanoparticles

Zailai Xie and Benjamin Frank have contributed equally to this work.

✉ Annette Trunschke
trunschke@fhi-berlin.mpg.de

1 Department of Inorganic Chemistry, Fritz-Haber-Institut der Max-Planck-Gesellschaft, Faradayweg 4-6, 14195 Berlin, Germany

2 Present address: College of Chemsitry, Fuzhou University, Qishan Campus, 2 Xueyuan Road, 350116 Fuzhou, People's Republic of China

3 Present address: BasCat - UniCat BASF JointLab, Technische Universität Berlin, Sekr. EW K 01, Hardenbergstr. 36, 10623 Berlin, Germany

1 Introduction

Higher alcohols (C_{2+}) are industrial key intermediates and low-emission fuels usually produced in multi-step processes [1, 2]. A direct route from syngas is highly desirable to cope with clean energy demands [1–5]. However, the Fischer-Tropsch (FT) approach so far fails in obtaining

higher alcohols with a sufficient selectivity at a high level of CO conversion [6, 7]. Considerable effort has been devoted to improving the catalyst performance by optimizing the active phases, adding promoters, and varying catalyst supports [1, 2, 4, 6, 8–10]. Model catalysts based on Rh exhibit a unique selectivity to oxygenates due to moderate ability for CO dissociation [6, 8, 10–13]. Here, a variety of transition metals were identified as efficient dopants, e.g., Mn, Fe, Co, Mo, or Zr [8, 14–16].

Besides the active phase, the support plays a key role in determining the alcohol productivity, e.g., by metal-support interaction, which governs the dispersion and stability of metal nanoparticles [17]. Several studies indicated that CNTs are more efficient supports for higher alcohol synthesis [8, 17–20] than conventional metal oxides such as Al_2O_3 [21], and SiO_2 [5, 9, 22]. On the other hand, N-doping of nanocarbons is known to efficiently increase the dispersion of noble metal nanoparticles [17, 23–25].

Here, we investigate the application of commercial N-doped CNTs as support for Rh-based catalysts in higher alcohol synthesis. It turned out that residual metal oxides in NCNTs have an impact on the catalytic performance of Rh by changing the catalyst under reaction conditions of CO hydrogenation.

2 Experimental

2.1 Catalyst Synthesis

We compared (1) CVD-grown commercial NCNTs (NCNT-1) [26], (2) pre-oxidized high-purity CNTs (OCNT), and (3) N-doped CNT, which were produced by NH_3 treatment of OCNT (NCNT-2) [27].

Unpurified CVD-grown NCNTs (NCNT-1; support ID 12836) have been received from Bayer Material Science [26].

Purified CNTs (Baytubes C150 HP®, carbon content >99 wt%, bulk density 140–230 kg m^{-3}) with 13 nm outer diameter and 4 nm inner diameter in average were obtained from Bayer Material Science. 20 g CNTs were treated in 1 L concentrated nitric acid (Carl Roth, 65 wt%, p.a.) under reflux for a period of 4 h. After cooling down to ambient temperature, the oxidized sample was thoroughly washed and filtrated with Millipore water until neutral pH. Finally, the resulting carbon was dried at 110 °C in static air for 3 days (OCNT; support ID 16603).

Nitrogen incorporation into purified oxidized CNTs was performed by treatment of 4 g OCNT in 50 % NH_3 in Ar at 150 mL$_n$ min^{-1} in a rotating tubular quartz reactor (40 mm inner diameter and 740 mm in length). The sample was heated at 5 °C min^{-1} to 500 °C. The target temperature was maintained for 6 h. Afterwards the sample was cooled down

to ambient temperature in the NH_3/Ar mixture (NCNT-2; support ID 17790).

Rh/N(O)CNTs catalysts were prepared by wet impregnation. 450 mg Rh(NO$_3$)$_3$ (10 % Rh, Sigma) was dissolved in 8 mL de-ionized water. The solution (pH 3) was then added to 1.5 g functionalized CNTs. Ultra-sonication was carried out for 1 min followed by evacuation at room temperature. The sample was reduced at 350 °C for 2 h in 20 % H_2 in Ar at a total flow of 100 mL min^{-1} resulting in the catalysts Rh/NCNT-1 (catalyst ID 15318), Rh/NCNT-2 (catalyst ID 18232), and Rh/OCNT (catalyst ID 17863), respectively.

RhCo/OCNT (catalyst ID 16999) and RhMn/OCNT (catalyst ID 16915) reference catalysts were prepared by wet impregnation using Rh(NO$_3$)$_3$, Co(NO$_3$)$_2$·6H$_2$O, and Mn(NO$_3$)$_2$·4H$_2$O as precursors and OCNT as support. The impregnation was performed in two steps starting with Rh, followed by reduction at 350 °C for 2 h in 20 % H_2/Ar gas mixture and subsequent impregnation with Co or Mn salts. Finally, the catalysts were reduced at second time at 350 °C for 2 h in 20 % H_2/Ar gas mixture.

2.2 Characterization of Supports and Catalysts

Scanning electron microscopy (SEM) images were obtained using a Hitachi S-4800 FEG microscope (1.5 kV) equipped with an EDAX Genesis EDX detector (15 kV). Transmission electron microscopy (TEM) bright field images were taken using a Philips CM200 microscope equipped with a LaB$_6$ cathode at an acceleration voltage of 200 kV. The nanostructure of supported metal particles was examined using a FEI aberration-corrected Titan 80–300 TEM microscope operated at 300 kV. For TEM analysis the samples were deposited onto holey carbon coated Cu grids without using a solvent. Particle size distributions have been obtained by analyzing 100 particles for Rh/NCNT-1, 200 particles for Rh/OCNT, and 125 particles for Rh/NCNT-2, respectively.

N_2 physisorption was performed at −196 °C in the range $p/p_0 = 0.05$–0.3 after drying the sample in vacuum at 120 °C for 6 h applying a volumetric N_2 physisorption apparatus (Autosorb-6-B, Quantachrome).

The XRD measurements were performed on a Bruker AXS D8 ADVANCE II diffractometer equipped with a nickel filter and a LYNXEYE position sensitive detector (Cu K$_{\alpha1+2}$ radiation) in Bragg-Brentano geometry (fixed divergence slit).

Temperature-programmed reduction (TPR) of the catalysts was performed in a quartz fixed-bed tubular reactor (TPDRO-1100, CE Instruments) in 5.04 % H_2/Ar (80 mL min^{-1} applying a heating rate of 5 K min^{-1}). The H_2 consumption was monitored using a thermal conductivity detector (TCD). The TCD detector was calibrated by reducing a known amount of CuO.

Analysis of the nitrogen content (CHN analysis) was done using a Thermo FlashEA 1112 NC Analyzer. The

metal content in the catalysts was analyzed by X-ray fluorescence spectroscopy (XRF) using a Bruker S4 Pioneer X-ray spectrometer.

Zeta potential measurements were performed using a Malvern Zetasizer. Approximately 5 mg of CNFs were dispersed in 100 mL deionized water and sonicated for 10 min. Thereafter, the suspensions were kept at 25 °C and the pH was adjusted manually using 0.1 M sodium hydroxide and hydrogen chloride, respectively, and the zeta potential was measured.

X-ray photoelectron spectroscopy (XPS) measurements were performed at ambient temperature under UHV conditions (base pressure $<3 \times 10^{-10}$ m bar) employing non-monochromated Al K_α radiation source (1486.6 eV). Spectra were acquired using a hemispherical analyzer (Phoibos 150, SPECS) operated in fixed analyzer transmission mode at a pass energy of 20 eV.

2.3 CO Hydrogenation

CO hydrogenation was carried out in a high-pressure set up. 800 mg of catalyst (powder, 200~400 µm) was loaded into a tubular stainless steel fixed bed reactor. The standard reaction conditions were: $p = 100$ bar, $H_2/CO = 1$, $T = 350$ °C, flow rate $= 10$ mL min^{-1}. The setup and the method of product analysis have been described elsewhere [28].

3 Results and Discussion

3.1 Characterization of the Supports

All supports have outer and inner diameters of 10–15 and 3–5 nm, respectively (see for example a representative SEM image of NCNT-1 in Fig. S1). Elemental composition and specific surface area of supports are listed in Table 1.

Chemical vapor deposition (CVD) over mixed metal catalysts (Mg, Al, Mn, Co) was used to produce NCNTs on kg scale [26]. During this process, finely dispersed metal

(oxide) nanoparticles remain in the raw product as impurities. Scanning electron microscopy (SEM) and transmission electron microscopy (TEM) images of NCNT-1 show many metal oxide particles being encapsulated by a thin carbonaceous layer (Supplementary material, Figure S1, representative SEM (top) and TEM (bottom) images of pristine NCNT-1). The co-existence of Mg, Al, Mn, and Co impurities in NCNT-1 was confirmed by X-ray fluorescence (Table 1). Although a substantial purification of N-free CNTs is feasible and typically achieved by refluxing in concentrated HNO$_3$, this approach fails for NCNTs due to the severe loss of surface N functional groups.

To disentangle the impact of nitrogen and metal doping, NCNTs derived from high-purity pre-oxidized CNTs (OCNT) have been included into the investigation. OCNT and NCNT-2 are free of metal impurities (Table 1).

The assembly of distinct nitrogen species at the surface of NCNT-1 and NCNT-2 was compared by X-ray photoelectron spectroscopy (Figure S2). Pyridinic nitrogen provides the lowest binding energy (BE) of 398.3 eV (N1). A peak at 399.2 eV (N2) is related to NH bonds in amides and amines. A feature at 400.1 eV (N3) indicates the presence of pyrrolic N, whereas the BE of 401.1 eV (N4) is typically referred to quaternary N species [29]. A peak at 402.1 eV is related to N-O bonds in pyridine-oxide or nitro groups (N5) [30]. Evidently, the surface properties of NCNT-1 and NCNT-2 differ in type (Figure S2) and amount (Table 1) of N-functionalization. Overall nitrogen content and relative abundance of pyridinic nitrogen are higher in NCNT-1.

3.2 Characterization of Rh Nanoparticles

The specific surface areas S_{BET} of the supports decrease upon Rh loading. However, fine dispersion of 2.5–2.6 wt% Rh is still possible (Fig. 1). The co-existence of Mg, Al, Mn, and Co impurities was also proven in Rh/NCNT-1 (Table 1). SEM (Fig. 1a, c, e), TEM, (Fig. 1b, d, f) and XRD analyses (Figure S3) confirm the dispersion of Rh, the entangled morphology of the (N)CNT samples, and the absence of large agglomerates of residual catalyst impurities in the supports and the reduced catalysts.

For Rh/NCNT-1 high-angle annular dark-field (HAADF) scanning TEM (STEM) reveals highly dispersed and homogeneously distributed Rh particles with a mean particle size of 1.4 nm (inset in Fig. 1a, b) after reduction in hydrogen at 350 °C. The high dispersion can be caused by the abundance of N-functionalities serving as anchoring sites on the surface of NCNT-1. A corresponding high-resolution TEM (HRTEM) image (Fig. 2a) shows lattice fringes with d-spacing of 0.22 nm, corresponding to the (111) planes of face-centered cubic (*fcc*) metallic Rh.

In the case of Rh/OCNT, HAADF-STEM shows larger Rh nanoparticles (2.7 nm) indicating a less ideal metal-support

Table 1 Elemental composition (wt%) and specific surface area (m^2 g^{-1}) of supports and catalysts

Sample	N[a]	Rh[b]	Metal impurities[b]				S_{BET}
			Mg	Al	Mn	Co	
NCNT-1	4.6	0	1.4	1.4	1.5	1.5	196
NCNT-2	1.2	0	–	–	–	–	324
OCNT	0	0	–	–	–	–	338
Rh/NCNT-1	4.2	2.5	1.1	1.2	1.6	1.8	175
Rh/NCNT-2	0.7	2.6	–	–	–	–	316
Rh/OCNT	0	2.6	–	–	–	–	234

[a]CHN analysis

[b]Analysed by X-ray fluorescence

Fig. 1 SEM (**a**, **c**, **e**) and HAADF-STEM (**b**, **d**, **f**) images, as well as particle size distribution (*insets*) of freshly reduced Rh/NCNT-1 based on 100 particles (**a**, **b**), Rh/OCNT based on 200 particles (**c**, **d**) and Rh/NCNT-2 based on 125 particles (**e**, **f**)
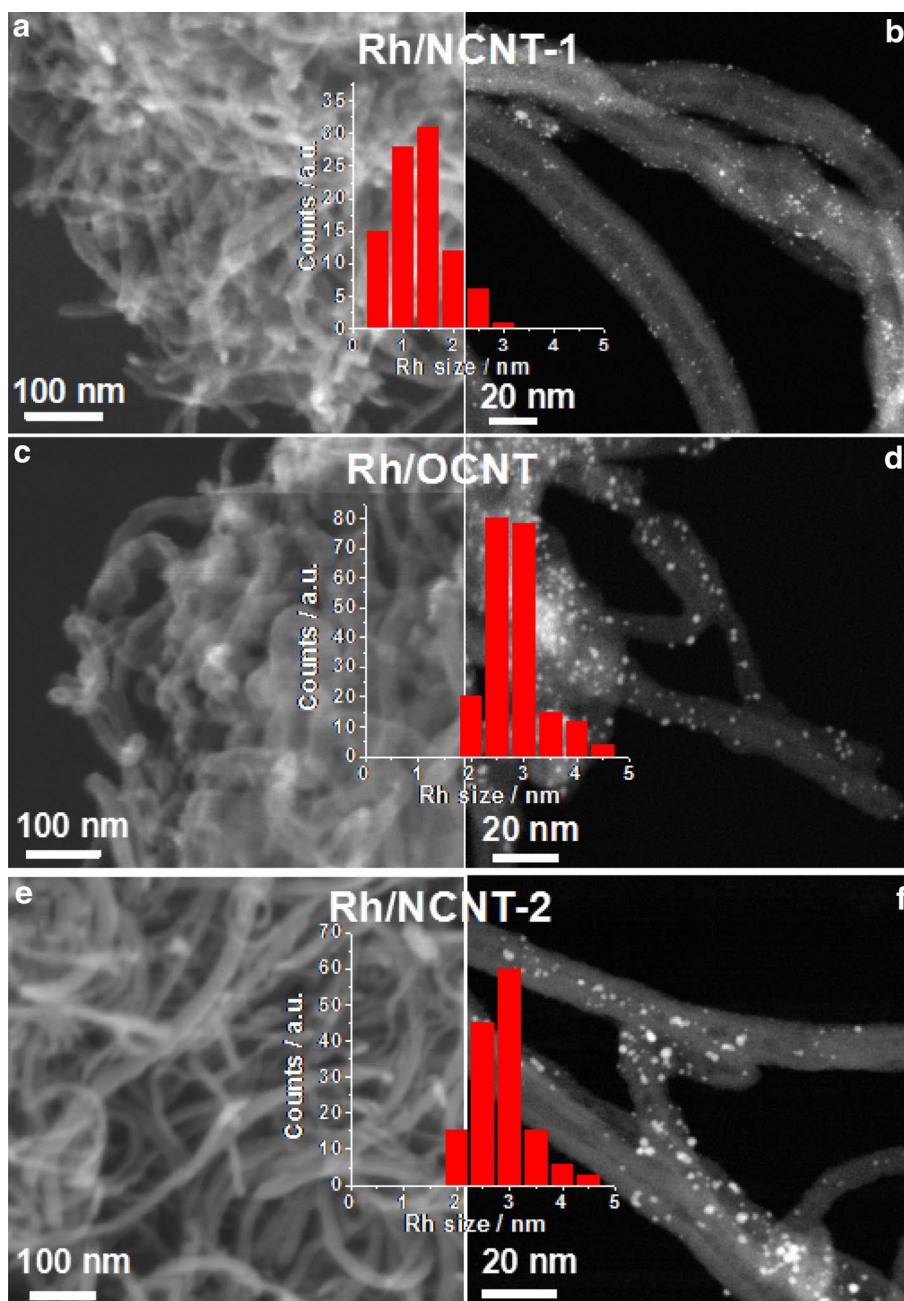
interaction, however, with a rather narrow particle size distribution (inset in Fig. 1c, d). The HRTEM analysis of a selected Rh particle in Rh/OCNT exhibits lattice fringes of *fcc* Rh (200) with a *d*-spacing of 0.19 nm (Fig. 2b).

The mean Rh particle size in Rh/NCNT-2 corresponds to 2.6 nm (inset in Fig. 1f, g).

Considering the abundance of acidic oxygen functionalities generated by HNO_3 oxidation of the CNTs, the trend in mean particle sizes can be correlated with the type and amount of surface functional groups (Table 1), which result in the isoelectric point of the different (N)CNT surfaces of 4.7, 3.8, and 2.8 for NCNT-1, NCNT-2, and OCNT, respectively (Figure S4).

For instance, the smaller Rh nanoparticles on NCNT-1 as compared to NCNT-2 might indicate an improved Rh-N interaction with pyridinic N species, leading to a better dispersion in the reduced catalyst. The similar particle size distribution in Rh/OCNT and Rh/NCNT-2 indicates that the relevant pyridinic N-content in NCNT-2 is apparently too low (as revealed by the larger Rh particles present in NCNT-2 compared to NCNT-1).

The temperature-programmed reduction (TPR) of the catalysts provides similar profiles of H_2 consumption (Figure S5) with a sharp peak at $166 \pm 2\,^{\circ}C$. The absolute consumption of H_2 at 40–330 °C corresponds to 0.40, 0.39, and 0.42 mmol g^{-1} for Rh/NCNT-1, Rh/NCNT-2, and Rh/
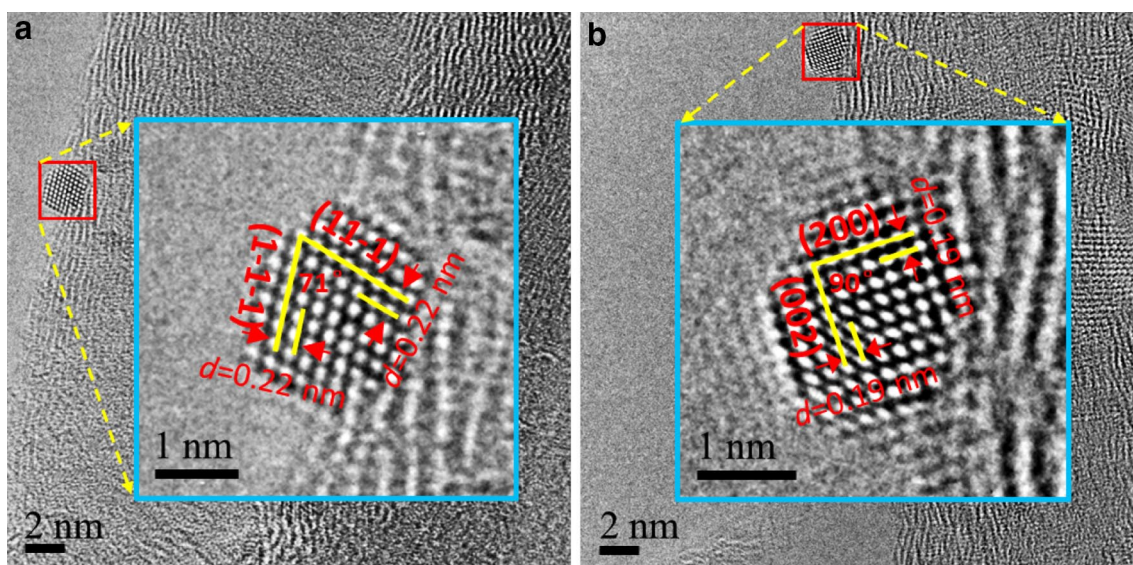
Fig. 2 HRTEM images of (**a**) Rh/NCNT-1 and (**b**) Rh/OCNT

OCNT, respectively, in agreement with the theoretical H_2 consumption of 0.37 mmol g^{-1}. Accordingly, Rh species in all catalysts are completely reduced in H_2 at 350 °C. The additional H_2 consumption at $T > 350$ °C could be referred to the reduction of N and O functional groups on the carbonaceous support, the hydrogenation of the CNTs, as well as partial reduction of Co and Mn species on Rh/NCNT-1, catalyzed by Rh [31].

3.3 Catalytic Properties

The catalysts were tested in $H_2/CO = 1$ at 350 °C and 100 bar for a period of 72 h (Fig. 3).

Among the Rh-free support materials only NCNT-1 shows a significant CO conversion of 7.9%, which is

Table 2 Catalytic performances after a reaction time of 72 h

Catalyst	X(CO) (%)	S (at% C)[a]					
		MeOH	C$_{2+}$ alc.	C$_{2+}$ oxy.	CH$_4$	C$_{2+}$ HC	CO$_2$
NCNT-1	7.9	–	–	–	19.6	11.4	75.6
NCNT-2	3	–	–	–	60	5	35
OCNT	3.5	–	–	–	62	6	36
Rh/NCNT-1	48.9	1	9.5	3.6	33.2	21.8	30.9
Rh/NCNT-2	23	2.3	8.1	6.6	15.8	21.1	46
Rh/OCNT	24.8	2.4	12.5	6.4	15.6	21.5	41.3
RhMn/OCNT	29.3	2.1	14.8	8.2	14.5	22.2	38.2
RhCo/OCNT	53	0.8	6.2	6.2	18	36.8	32

[a]*alc.* alcohols, *oxy.* oxygenates, *HC* hydrocarbons

Fig. 3 Conversion of CO (**a**), and yield of higher alcohols (**b**) as a function of time on stream, $H_2/CO = 1.0$, 100 bar, 350 °C
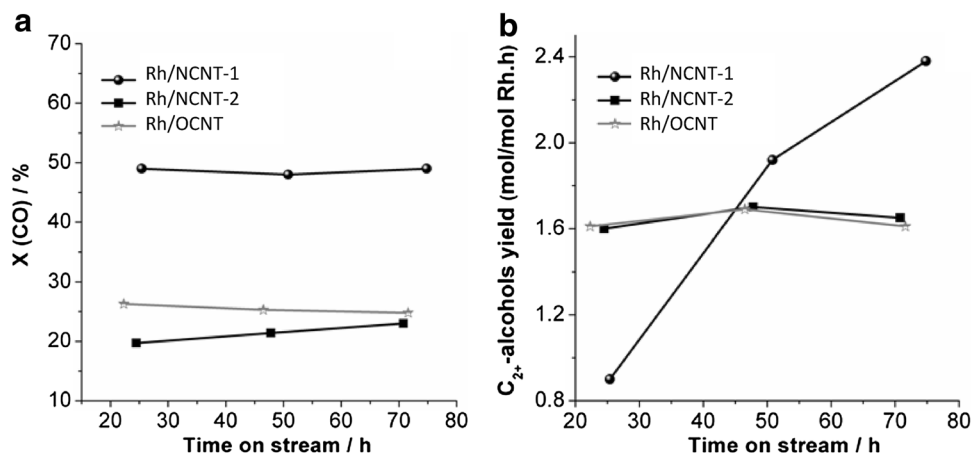
more than twice as much as the conversion on NCNT-2 and OCNT (Table 2). Carbon dioxide is the main product over commercial NCNT-1, whereas CH_4 is predominantly formed over NCNT-2 and OCNT, respectively. Perhaps, the residual catalyst impurities in NCNT-1 are not only active in CO hydrogenation to short-chain alkanes, but also show activity in the consecutive water–gas shift reaction.

Rh/NCNT-1, Rh/NCNT-2, and Rh/OCNT show a fairly stable CO conversion within a reaction time of 72 h (Fig. 3a). However, Rh/NCNT-1 not only outperforms the other catalysts in terms of CO conversion but also results in the highest yield of C_{2+} alcohols, by trend even remarkably increasing after 72 h time on stream (Fig. 2b). This indicates that the catalyst is changing with time on stream.

Rh/NCNT-1 shows a C_{2+} alcohol selectivity of 9.5 % at a CO conversion of 48.9 %, which corresponds to a formation rate of 2.4 mol mol_{Rh}^{-1} h^{-1} (Table 2). Notably, this catalyst provides also the highest formation rate of CH_4, whereas Rh/NCNT-2 and Rh/OCNT show increased selectivity to CH_3OH, C_{2+} oxygenates, and CO_2. However, regarding the chain length distribution of alcohols formed (Figure S6), Rh/NCNT-1 produces predominantly C_2H_5OH, whereas the spectrum is significantly shifted to C_{3+} alcohols over Rh/OCNT.

Although all catalysts appeared stable in terms of CO conversion over a reaction time of 72 h, a significant sintering of Rh nanoparticles was observed (Fig. 4) compared to the dispersion in the fresh catalysts after reduction (Fig. 1). The enhanced sintering of Rh particles can be partially related to the loss of N functional groups during the catalytic reaction, as confirmed by elemental analysis (Table S1). The partial loss of N functionalities likely occurs via Rh-catalyzed hydrogenation under CO hydrogenation reaction conditions. Similarly, the TPR profiles showed a broad H_2 consumption peak starting at 350 °C, which was referred to the reduction of surface N and O functionalities. Also the formation of volatile Rh carbonyl clusters can play a role in

the sintering process, which, however, is not detrimental for the net reactivity of the catalyst.

The increase in C_{2+} oxygenate productivity with time on stream over Rh/NCNT-1 can be explained by modification of the active component Rh with impurities originating from the support. Notably, Rh-Co alloy formation is identified in used Rh/NCNT-1 (Fig. 5) with Co originating apparently from the catalyst used for synthesis of the NCNT-1 support. Mass transfer most likely occurs via volatile carbonyl clusters. The final Co concentration in the alloy is approx. 30 %. The ongoing increase in C_{2+} alcohols productivity even after 72 h on stream (Fig. 3b) indicates that this process is still not equilibrated. Other residual elements such as Mn and Mg remain in the support, but may also influence the catalytic properties.

The positive impact of transition metal doping on Rh based catalysts for C_2H_5OH selectivity and higher alcohols has been numerously reported, for example [8, 32–35]. As discussed above even low amounts of metal impurities used for the CVD growth of CNTs are unavoidable, in spite of post-purification by acid or base treatment. Considering the abundance of residual Mn and Co species in NCNT-1, a positive impact on both activity and product spectrum is likely. For reference, we prepared Co and Mn doped Rh/OCNT catalysts to get insight into the mode of action of these additives. RhCo/OCNT and RhMn/OCNT were synthesized via a sequential impregnation method. Both samples provide highly dispersed and homogeneously distributed nanoparticles (Figure S7), similar to that of Rh/OCNT. The Co and Mn modified samples are similarly stable with time-on-stream. The corresponding reactivity patterns after a reaction time of 72 h are listed in Table 2. Considering the reduced Rh content (nominally 2 wt% as compared to 3 wt% in Rh/OCNT), a certain increase in activity is observed for the Mn doped catalyst, whereas the selectivity is only weakly shifted to C_{2+} alcohols/oxygenates. In total, Mn doping results in an increase of C_{2+} alcohol productivity from 1.6 to
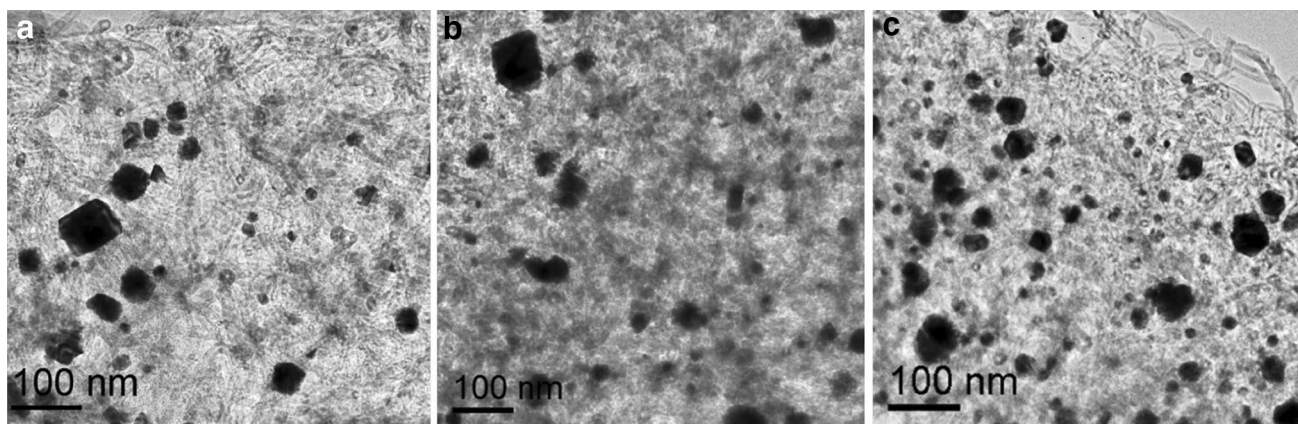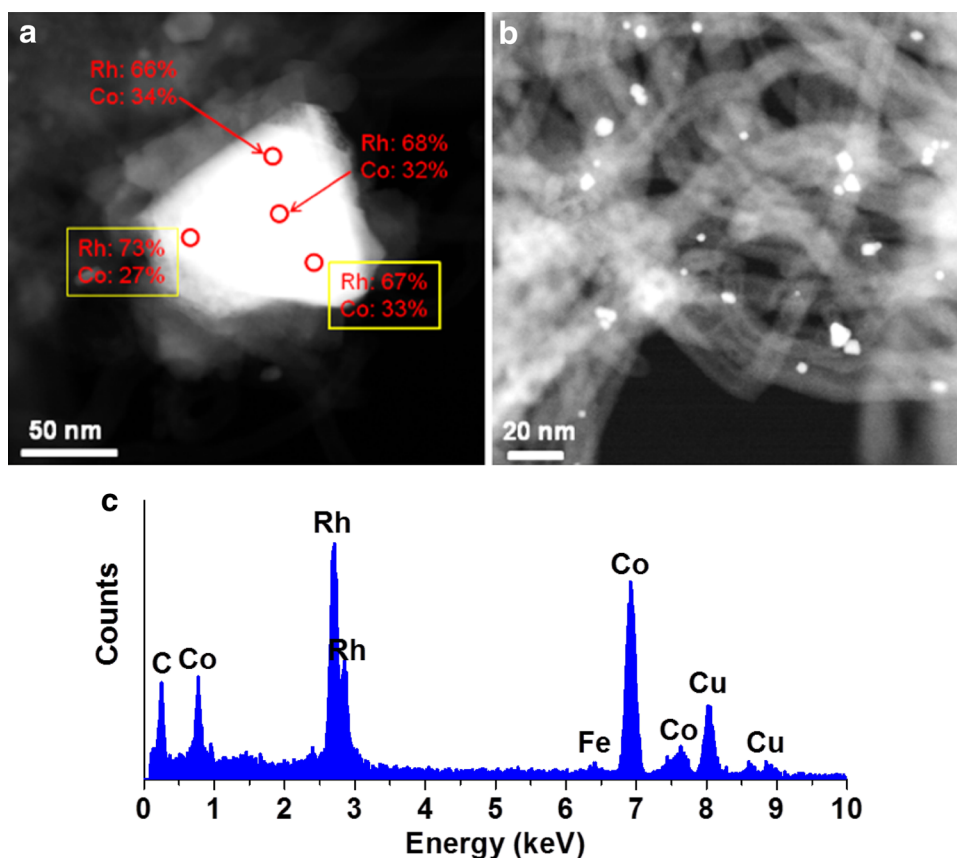

Fig. 4 TEM images of Rh/NCNT-1 (**a**), Rh/NCNT-2 (**b**), and Rh/OCNT (**c**) after reaction

Fig. 5 HAADF-TEM images of an extra-large particle in used Rh/NCNT-1 and EDX analysis of used Rh/NCNT-1. Occurrence of Cu is due to the TEM grid

3.3 mol mol_{Rh}^{-1} h^1, in agreement with literature reports [8, 32, 33]. Instead, RhCo/OCNT shows a significantly higher CO conversion of 53 %, however, a reduced selectivity to oxygenates. The total productivity of C_{2+} alcohols remains stable at 1.6 mol mol_{Rh}^{-1} h^{-1}. Instead, the product spectrum is dominated by CH_4 and lower alkanes, in agreement with the finding that Co promotes the dissociation of CO to greatly increase the activity and enhance the selectivity to higher alkanes [34–37].

Notably, earlier reports revealed that CNT or metal oxide supported non-promoted Rh catalysts provide a poor activity to higher alcohols (C_{3+}) [4, 8, 13]. Considering the high purity of OCNT and NCNT-2 in our study in terms of residual metal, the significant formation of higher alcohols over both Rh/OCNT and Rh/NCNT-2 might be related to the high pressure applied in our tests, which shifts the equilibrium of alcohol formation via CO hydrogenation to the product side [3].

4 Summary

Supporting Rh nanoparticles on commercial N-doped CNTs containing residual Co and Mn from the CVD growth process results in an active and selective catalyst for the synthesis of higher alcohols. The catalysts are highly stable with time-on-stream although significant sintering of nanoparticles is observed. A dedicated assembly of surface N functionalities efficiently stabilizes the active phase to form homogeneously distributed and finely dispersed Rh nanoparticles in the fresh catalyst. A direct influence of the electronic structure of N-doped CNTs on the catalytic action of Rh active sites is likely, however, could not be proven in this study. Loss of nitrogen is observed under the applied reaction conditions.

Instead, residual Co and Mn present as impurities in the support efficiently promote the catalyst and results in both increased activity and selectivity to C_{2+} alcohols by modification of the active Rh component under reaction conditions of CO hydrogenation. It is assumed that the formation of Rh-Co alloy is the key factor for enhanced activity, whereas the interaction with Mn species results in an enhanced selectivity to oxygenates. This report exemplifies the resource efficient use of a commercial nanocarbon for synthesis of promoted Rh catalysts avoiding additional purification and impregnation steps.

References

1. Xiao K, Qi XZ, Bao ZH, Wang XX, Zhong LS, Fang KG, Lin MG, Sun YH (2013) Catal Sci Technol 3:1591–1602
2. Lu Y, Cao B, Yu F, Liu J, Bao Z, Gao J (2014) ChemCatChem 6:473–478
3. Spivey JJ, Egbebi A (2007) Chem Soc Rev 36:1514–1528
4. Haider MA, Gogate MR, Davis RJ (2009) J Catal 261:9–16
5. Yu J, Mao DS, Han LP, Guo QS, Lu GZ (2013) J Mol Catal A 367:38–45
6. Chuang SSC, Stevens RW, Khatri R (2005) Top Catal 32:225–232
7. Galvis HMT, de Jong KP (2013) ACS Catal 3:2130–2149
8. Pan XL, Fan ZL, Chen W, Ding YJ, Luo HY, Bao XH (2007) Nat Mater 6:507–511
9. Gao J, Mo XH, Goodwin JG (2011) Catal Today 160:44–49
10. Chai SH, Howe JY, Wang XQ, Kidder M, Schwartz V, Golden ML, Overbury SH, Dai S, Jiang DE (2012) Carbon 50:1574–1582
11. Wang HY, Liu JP, Fu JK, Wan HL, Tsai KR (1992) Catal Lett 12:87–96
12. Vannice MA, Ollis DF (1982) J Catal 78:266–266
13. Mavrikakis M, Baumer M, Freund HJ, Norskov JK (2002) Catal Lett 81:153–156
14. Yan Z, Bukur DB, Goodman DW (2011) Catal Today 160:39–43
15. Wijayapala R, Yu F, Jr CUP, Mlsna TE (2014) Appl Catal A 480:93–99
16. Johnson GR, Bell AT (2016) ACS Catal 6:100–114
17. Lu JZ, Yang LJ, Xu BL, Wu Q, Zhang D, Yuan SJ, Zhai Y, Wang XZ, Fan YN, Hu Z (2014) ACS Catal 4:613–621
18. Kang JC, Zhang SL, Zhang QH, Wang Y (2009) Angew Chem 48:2565–2568
19. Schulte HJ, Graf B, Xia W, Muhler M (2012) ChemCatChem 4:350–355
20. Becker MJ, Xia W, Tessonnier JP, Blume R, Yao LD, Schlögl R, Muhler M (2011) Carbon 49:5253–5264
21. Ojeda M, Rojas S, Garcia-Garcia FJ, Granados ML, Terreros P, Fierro JLG (2004) Catal Commun 5:703–707
22. Zhou ST, Zhao H, Ma D, Miao SJ, Cheng MJ, Bao XH (2005) Z Phys Chem 219:949–961
23. Villa A, Wang D, Spontoni P, Arrigo R, Su DS, Prati L (2010) Catal Today 157:89–93
24. Arrigo R, Schuster ME, Wrabetz S, Girgsdies F, Tessonnier JP, Centi G, Perathoner S, Su DS, Schlögl R (2012) ChemSusChem 5:577–586
25. Lv RT, Cui TX, Jun MS, Zhang Q, Cao AY, Su DS, Zhang ZJ, Yoon SH, Miyawaki J, Mochida I, Kang FY (2011) Adv Funct Mater 21:999–1006
26. Wolf A, Michele V, Mleczko L, Assmann J, Buchholz S (2010) US Patent 20100276644
27. Arrigo R, Hävecker M, Wrabetz S, Raoul B, Lerch M, McGregor J, Parrott EPJ, Zeitler JA, Gladden LF, Knop-Gericke A, Schlögl R, Su DS (2010) J Am Chem Soc 132:9616–9630
28. Frank B, Xie Z-L, Trunschke A (2013) Chemie Ingenieur Technik 85:1290–1293
29. Jansen RJJ, Vanbekkum H (1995) Carbon 33:1021–1027
30. Chambrion P, Suzuki T, Zhang ZG, Kyotani T, Tomita A (1997) Energy Fuel 11:681–685
31. Tomita A, Tamai Y (1972) J Catal 27:293–300
32. Wilson TP, Kasai PH, Ellgen PC (1981) J Catal 69:193–201
33. Liu J, Tao R, Guo Z, Regalbuto JR, Marshall CL, Klie RF, Miller JT, Meyer RJ (2013) ChemCatChem 5:3665–3672
34. Kusama H, Okabe K, Sayama K, Arakawa H (2000) Appl Organomet Chem 14:836–840
35. Kiviaho J, Reinikainen M, Niemelä MK, Kataja K, Jääskeläinen S (1996) J Mol Catal A 106:187–195
36. Iglesia E (1997) Appl Catal A 161:59–78
37. Khodakov AY, Chu W, Fongarland P (2007) Chem Rev 107:1692–1744